

# Deep Convolutional Neural Networks for Bias Field Correction of Brain Magnetic Resonance Images

YAN XU<sup>1,2</sup>, SHUNBO HU<sup>2</sup>, YUYUE DU<sup>1</sup>

<sup>1</sup>College of Computer Science and Engineering, Shandong University of Science and Technology, Qingdao 266590, China

<sup>2</sup>College of Information Science and Engineering Linyi University Shandong Province 276005, China

Corresponding author: Yuyue Du ([yydu001@163.com](mailto:yydu001@163.com)), Shunbo Hu ([hushunbo@lyu.edu.cn](mailto:hushunbo@lyu.edu.cn))

**Abstract** As a low-frequency and smooth signal, the bias field has a certain destructive effect on magnetic resonance(MR) images, and is the main obstacle for doctors' diagnosis and image processing (such as segmentation, texture analysis, and registration). Before analyzing a damaged MR image, a preprocessing step is needed to correct the bias field in the image. Unlike traditional bias field removal algorithms based on signal models and a priori assumptions, deep learning methods do not require precisely modeling signals and bias fields, and do not need to adjust parameters. After the large training set is trained through the deep neural network, the MR image with the bias field is input, and the corrected MR image is output. In this paper, we propose taking the local feature images of the bias field in multiple frequency bands obtained by the log-Gabor filter bank and the original image as input, correct the bias field of a brain magnetic resonance image through a deep separable convolutional neural network, and use residual learning and batch normalization to speed up the training process and improve bias field correction performance. Our training model was tested on the BrainWeb simulated database and HCP real dataset, and the results of the qualitative analysis show that our training model achieved better performance than the traditional state-of-the-art N4 and NIMS (Non-Iterative Multi-Scale) methods.

**Keywords:** Magnetic resonance imaging; Intensity inhomogeneity correction; Bias field; Log-Gabor filter; Deep learning

## 1 Introduction

Among the many image acquisition technologies, magnetic resonance imaging (MRI), as a noninvasive medical imaging technology, has the characteristics of high resolution and high contrast in soft tissues and plays an important role in diagnosing the pathology of human internal tissues and organs. Especially in brain image research, MRI is superior to other imaging techniques. However, in the MRI imaging process, due to the influence of factors such as the uneven static magnetic field, the eddy current formed by the gradient field, and the uneven sensitivity of the receiving coil, MRI will have uneven intensity. This phenomenon is called MR image artifacts and is, also known as the bias field. The bias field is a poor low-frequency smooth signal (as shown in Fig. 1), and it will change the intensity value of the pixel, which makes the same tissue in the image have a different intensity distribution. The existence of the bias field may affect the accuracy of clinical diagnosis and reduce the performance of quantitative image processing (such as segmentation, registration and classification) algorithms. Therefore, before further processing an image, the bias field of the

MR image must be eliminated.

In past research, a variety of correction methods for the bias field have been proposed [1]. According to the different sources of the bias field, the correction methods are mainly divided into two types: prospective methods [2,3] and retrospective methods [4,5]. Prospective methods,

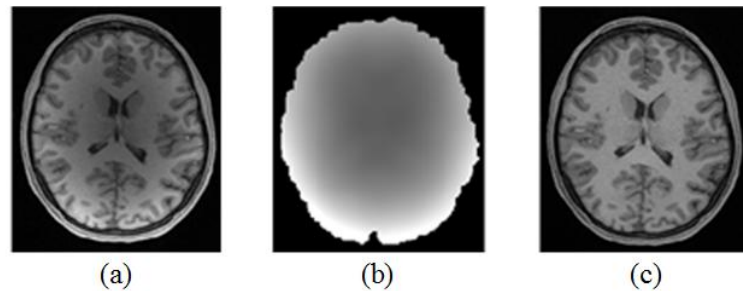


Fig. 1 Bias field in MR brain image. (a) Original image (b) Bias field (c) Corrected image

such as model-based calibration [6], and multicoil imaging [7–8], mainly correct the bias fields caused by specific nuclear magnetic resonance equipment. This method can only handle the bias fields caused by equipment and environmental reasons, but cannot handle the bias fields introduced by the patients. Retrospective methods are image-based postprocessing methods. They are correction methods proposed for the bias field generated by the shape, position, direction and specific magnetic permeability of an imaged object. They do not distinguish the source of a bias field, and are only based on the image intensity and prior knowledge of an imaging object [9]. Retrospective strategies mainly include methods based on filtering [10–11], surface fitting [12–15], segmentation [16–19] and histograms [20–22]. These methods mainly rely on the information of the acquired image and use prior knowledge about the spatial relationships of the imaged anatomical structure and/or intensity probability distribution to extract the hidden bias field in the image [23]. Retrospective methods usually make some assumptions about the acquisition process and can handle the bias field artifacts related to the scanner and anatomy. Compared with prospective methods that can only correct bias fields caused by MR scanning equipment, retrospective methods can also eliminate the bias fields introduced by patients.

The N4 bias correction method proposed by Tustison et al. [24] is currently the most popular and widely used bias correction method. It uses a robust B-spline approximation procedure and an improved hierarchical optimization method for bias field correction [25]. This method requires foreground extraction, and the bias removal efficiency may depend on the background removal accuracy, the initialization of the width of the bias field histogram and the spline distance [26]. When the method is executed in ITK (The Insight Segmentation and Registration Toolkit), it is time-consuming. George et al. [26] proposed a new method for correcting intensity nonuniformity using non-iterative multi-scale (NIMS) method in 2017. This method does not need to segment an image, nor does it need to have any prior knowledge of the scanner or the subject, and it extracts the bias field by using the log-Gabor filter bank to perform multiscale analysis on the input image. The NIMS method does not require iteration, so the running time is relatively short; however it easily causes filtering artifacts in the high-contrast area of brain images, and it is not effective at removing the biases of brain images with serious pollution.

Although both prospective and retrospective methods have achieved good performance in the removal of bias fields, they still have some shortcomings, including the needs to model the signal and bias fields, manually set parameters, and optimize methods in the test phase, etc. Recently, as

the architecture has become more flexible, deep learning techniques have gained the ability to overcome these shortcomings [27]. Therefore, in this paper, we use deep learning to build a bias removal network (BiasNet) to correct the bias field of brain magnetic resonance images.

In order to obtain more local contrast information of the bias field, before conducting network training, we first use the log-Gabor filter bank to extract the local feature map of the bias field located in multiple frequency bands from a T1 image and take the local feature map and the original image as the input of the network. Then, deep separable convolution is introduced in BiasNet to obtain more pixel-level features, residual learning and batch normalization are used to speed up the training process, and BiasNet can automatically conduct deep learning to obtain a more accurate bias field. We tested the model proposed in this paper on the dataset of different INU (intensity nonuniformity) levels of the SBD (Simulated Brain Database) and the real HCP (Human Connectome Project) dataset. The results of the qualitative analysis show that the training model proposed in this paper achieves better performance than the traditional state-of-the-art N4 and NIMS methods.

## 2. Log-Gabor filter bank

The Gabor filter, as a statistical image local information extraction method, has good multi-channel and multi-resolution characteristics, but it is not a bandpass filter in the strict sense. When the bandwidth is greater than 1 octave, even part of the Gabor filter will produce non-DC components, so the bandwidth of the Gabor filter can only be limited to the 1 octave range [28]. If you want to obtain wider spectrum coverage, you need to use many Gabor filters, and the amount of calculation will be greatly increased. David J. Field introduced the log-Gabor filter in 1978 to solve the nonzero DC component in the Gabor filter at a higher bandwidth [29]. In addition to the advantages of the Gabor filter, the log-Gabor filter also compensates for some of its shortcomings [28]: (1) log-Gabor filter has no DC component and the bandwidth is not limited; (2) the transfer function of the log-Gabor filter has an extended tail at the high-frequency end, which is more effective for natural image encoding than the Gabor function that overrepresents low-frequency components; and (3) the log-Gabor function's measurement of the logarithmic frequency scale is consistent with that of the human visual system.

Due to the singularity of the logarithmic function at the origin, the response function of the log-Gabor filter cannot be represented in the spatial domain, but the filter can be constructed in the frequency domain. The polar coordinate expression of the two-dimensional log-Gabor filter function in the frequency domain is [30]:

$$G(\omega, \theta) = G_\omega \times G_\theta, \quad (1)$$

$$G_\omega = \exp\left(\frac{-\left(\ln\left(\frac{\omega}{\omega_0}\right)\right)^2}{2\left(\ln\left(\frac{\sigma_\omega}{\omega_0}\right)\right)^2}\right), \quad G_\theta = \exp\left(-\frac{(\theta - \theta_0)^2}{2\sigma_\theta^2}\right)$$

where  $G_\omega$  is the radial component;  $G_\theta$  is the direction component;  $\omega_0$  and  $\theta_0$  are the center frequency of the filter and the direction of the filter, respectively;  $\omega$  and  $\theta$  are the frequency and

direction of the image to be filtered, respectively; and  $\sigma_\omega/\omega_0$  takes a value between 0 and 1. When constructing the filter bank, as  $\omega_0$  changes, the value of  $\sigma_\omega$  must be adjusted to keep their ratio constant, so as to achieve a constant shape ratio filter. The bandwidth  $B_\omega$  of the filter depends on the value of  $\sigma_\omega/\omega_0$ ,  $B_\omega = 2\sqrt{2/\ln 2} \cdot |\ln(\sigma_\omega/\omega_0)|$ , and the bandwidth direction  $B_\theta$  is determined by  $\sigma_\theta, B_\theta = 2\sigma_\theta\sqrt{2 \ln 2}$ . Fig. 2 and Fig. 3 are the images of the 2D Gabor function and the 2D log-Gabor function in the frequency domain and the spatial domain, respectively.

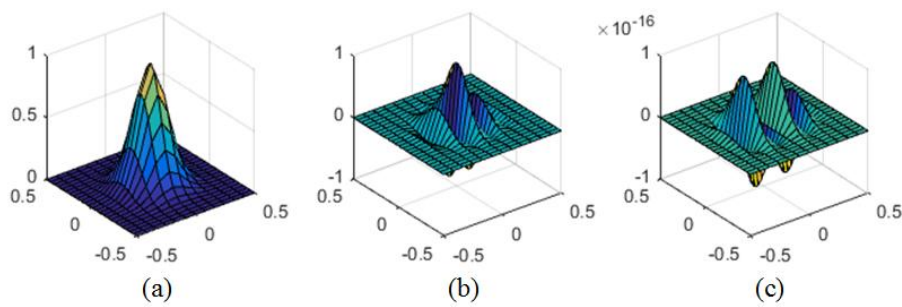


Fig. 2 The function images of 2D Gabor transformation in frequency domain and spatial domain. (A) image of Gabor transformation in frequency domain (b) Gabor even function image in spatial domain (c) Gabor odd function image in spatial domain

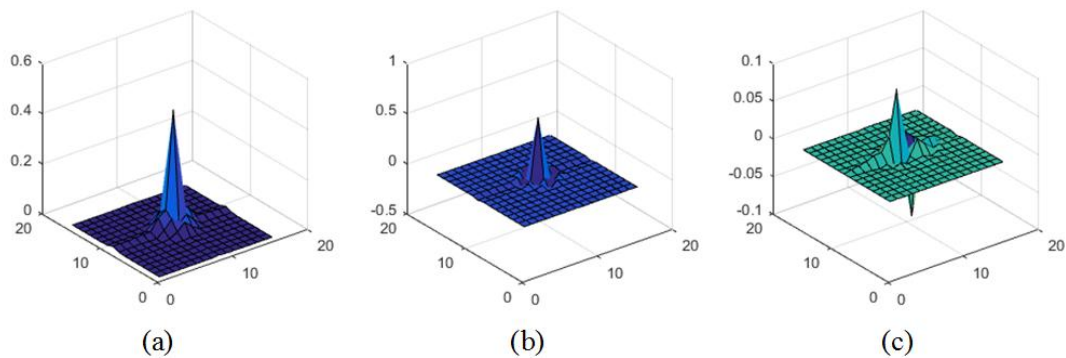


Fig. 3 The function images of 2D log-Gabor transformation in frequency domain and spatial domain. (A) image of log-Gabor transformation in frequency domain (b) log-Gabor even function image in spatial domain (c) log-Gabor odd function image in spatial domain

Fig. 2 and Fig. 3 show that the 2D log-Gabor filter and 2D Gabor filter have relatively similar function images in the spatial domain, which indicates that the 2D log-Gabor filter not only inherits the multi-resolution and multi-channel advantages of the Gabor filter [31] but also compensates for its lack of bandwidth. By constructing the log-Gabor filter bank, the local feature information of the image can be extracted from filters with different directions and different center frequencies.

The extraction of the bias field has high requirements for frequency and spatial positioning. The log-Gabor filter can provide any bandwidth to ensure better spatial positioning [32]. The log-Gabor filter bank can achieve frequency positioning through a set of tuned log-Gabor filters. Therefore, we choose log-Gabor function to construct a log-Gabor filter bank to extract the local

feature information of a bias field. The 3 octave bandwidth contains a large range of frequency components, which increases the difficulty of separating the bias field information from the decomposition band, and the 2 octave bandwidth can ensure that a smaller number of filters are used to effectively extract all frequency bands with deviation fields [26]. Therefore, each Gaussian filter in the filter bank uses the best bandwidth of 2 octave bands, namely  $B_\omega = 2\sqrt{2/\ln 2} \cdot |\ln(\sigma_\omega/\omega_0)| = 2$  octaves. Therefore, in order to maintain the bandwidth of the 2-octave filter, when  $\omega_0$  changes, the scale factor  $\sigma_\omega$  must be adjusted to keep the ratio

$$\frac{\sigma_\omega}{\omega_0} \text{ constant.}$$

We construct a filter bank composed of three tuned discrete log-Gabor filters, and the transfer function of the filter bank is shown in Formula (2). The filters are arranged in descending order of cutoff frequency. Among the three filters, the one with the smallest cutoff wavelength has the largest spectral radius in the frequency domain.

$$G(\omega_i, \theta_i) = G_{\omega_i} \times G_{\theta_i}, \quad i = 1,2,3 \quad (2)$$

$$G_{\omega_i} = \exp\left(\frac{-\left(\ln\left(\frac{\omega}{\omega_i}\right)\right)^2}{2\left(\ln\left(\frac{\sigma_\omega}{\omega_i}\right)\right)^2}\right), \quad G_{\theta_i} = \exp\left(-\frac{(\theta - \theta_i)^2}{2\sigma_\theta^2}\right)$$

Because  $B_\omega = 2\sqrt{2/\ln 2} \cdot |\ln(\sigma_\omega/\omega_i)| = 2$  octaves,  $\frac{\sigma_\omega}{\omega_i}$  must maintain a constant ratio

$$\frac{\sigma_\omega}{\omega_i} = e^{-\frac{(\sqrt{\ln 2}/\sqrt{2})}{\sqrt{2}}} = 0.55.$$

The local feature maps obtained after applying the log-Gabor filter bank to the T1w image from SBD are shown in Fig. 4.

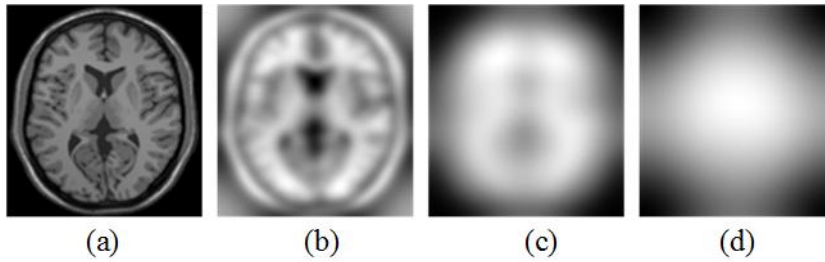


Fig. 4 Local feature maps obtained after applying log-Gabor filter bank on BrainWeb T1w image. (A) T1w image with 0% noise and 40% INU (b) Log-Gabor scale 1 output (c) Log-Gabor scale 2 output (d) Log-Gabor scale 3 output

### 3. Theory and Method

With a deeper network architecture, the deep learning-based method can expand the receptive field of a network to obtain a larger range of contextual information of an image, thereby obtaining

a more accurate bias field. Convolutional neural networks (CNNs) have been rapidly developed in image classification and segmentation since 2010 and have achieved great success [31]. The denoising convolutional neural networks (DnCNNs) using residual learning strategies proposed by Zhang et al. have achieved good performance [34]. A deep convolutional network (SRCNN) for image superresolution proposed by Dong et al. realized the conversion from low-resolution images to high-resolution images [35]. At present, there are few papers that use deep learning to remove the bias field in an image. We first introduce a simple and widely used mathematical model of a bias field [26]:

$$f(x) = u(x)b(x) + n(x) \quad (3)$$

Where  $f(x)$  is a contaminated image;  $u(x)$  is the real image;  $b(x)$  is the bias field; and  $n(x)$  represents the high-frequency noise introduced due to the defect of the MRI scanner, which is considered to be independent of the bias field. Assuming that  $n(x)$  follows a Gaussian probability distribution [36,37], it can be removed by conventional low-frequency filtering. In the current work, no explicit preprocessing of additive noise is considered. Therefore, Formula (3) can be simplified as:

$$f = u * b \quad (4)$$

$u$  is the desired signal,  $f$  is the contaminated signal, and  $b$  is the bias field. The basic idea of DL (deep learning) based on a NN (neural network) is to use the following formula to obtain the predicted bias field signal:

$$\hat{b} = Net(f; \theta) \quad (5)$$

Where Net represents the NN architecture and is a network parameter, including weights and biases. Therefore, the predicted real image can be obtained, and the multiplicative noise contained in the image is also removed. In this section, we will introduce the network architecture and how to optimize the parameters.

### 3.1 BiasNet architecture

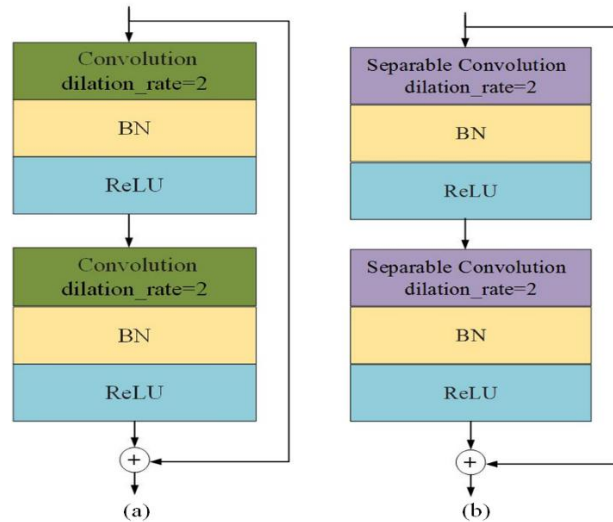


Fig. 5 Structure diagram of component CR and component SCR. (a) Structure diagram of component CR (b) Structure diagram of component SCR

Contextual information is very important for the reconstruction of pixels destroyed by the bias field. The deep learning-based method mainly captures more global contextual information by expanding the receptive field [38]. Although increasing the depth and width of the deep network can expand the receptive field, when the depth of the network is very large, continuing to increase the depth of the network may lead to the disappearance of the gradient, and the use of widening methods may generate more parameters, resulting in network overfitting. Therefore, we set the dilation rate to 2 in the convolutional layer of the convolution residual (CR) component or separable convolution residual (SCR) component of BiasNet and use the dilated convolution to extract global features, as shown in Fig. 5.

The CR component consists of the dilated convolution, residual learning, batch normalization (BN) and ReLU functions. The SCR component consists of separable expanded convolution, residual learning, batch normalization (BN) and ReLU functions. Residual learning fundamentally breaks the symmetry of the network and improves the ability to characterize the network. Moreover, a residual network is easier to optimize, and better accuracy can be obtained from the greatly increased depth [39]. By setting the BN layer, the generalization ability of the network is improved.

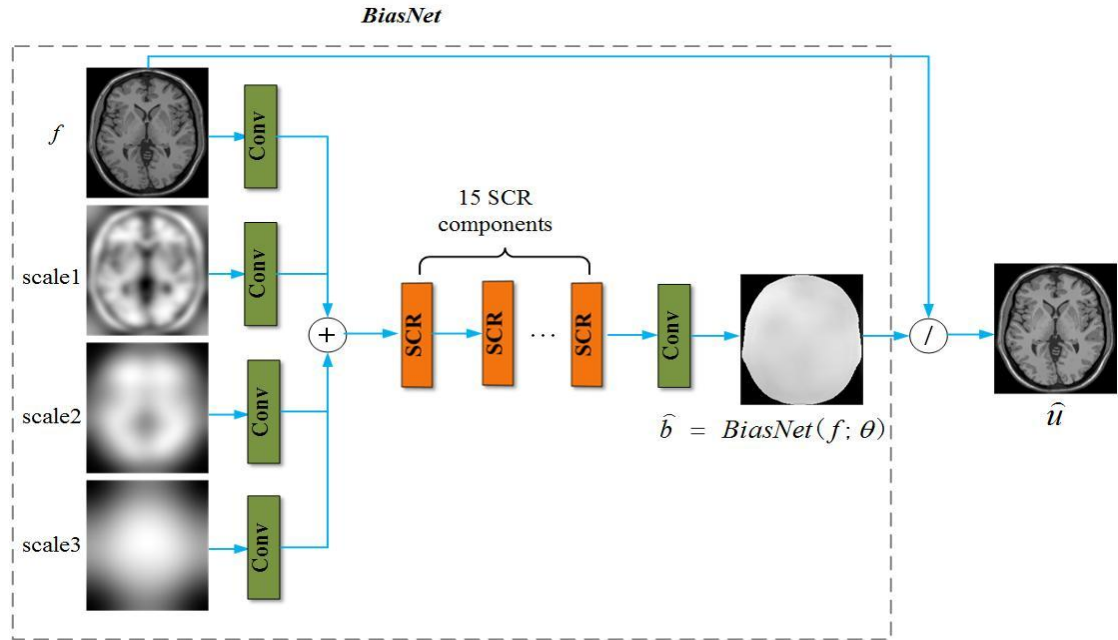


Fig. 6 Flow chart of bias removal in MR image based on the proposed BiasNet network structure.

BiasNet does not directly output an unbiased image but is used to predict the bias  $\hat{b}_{ij}$  at each pixel  $f_{ij}$  of the original image. Therefore, according to Formula (4), the unbiased intensity can be

calculated as  $\frac{f_{ij}}{\hat{b}_{ij}}$ . The process of MR image bias removal under this architecture is shown in

Fig. 6.

BiasNet has 4 input layers, which are the original image T1w and the feature images of scale 1, scale 2, and scale 3 from the log-Gabor filter bank. Each input layer extracts features through a convolutional layer with a  $3 \times 3$  convolution kernel and 64 filters and then uses an addition layer

to perform feature fusion. Subsequently, 15 SCR components are cascaded. The convolution kernel of each SCR component is  $3 \times 3$  and there are 64 filters. In order to expand the receptive field, the dilation rate is set to 2. Finally, through a  $1 \times 1$  convolution layer, a bias field image of the same size as the input is generated, and an unbiased image can be obtained by using the formula. The combination of residual learning and batch normalization in the SCR (CR) component speeds up the training speed and improves the bias removal performance. Because the output should have the same size as the input, the network does not have a pooling layer.

### 3.2 Optimization of BiasNet

In order to optimize the parameter  $\theta$  of the proposed BiasNet, the total loss function is defined as:

$$L = \alpha * Loss_{mse} + \beta * Loss_{dissim} \quad (6)$$

where  $Loss_{mse}$  is the mean squared error (MSE) function between the desired bias image and the estimated image from the input pollution image. It is defined as follows:

$$Loss_{mse} = \frac{1}{N} \sum_{i=1}^N \left( Net(f_i; \theta) - \left( \frac{f_i}{u_i} \right) \right)^2. \quad (7)$$

$Loss_{dissim}$  is the average structural difference function between the estimated bias field image and the desired bias field image and is defined as follows:

$$Loss_{dissim} = \frac{1}{N} \sum_{i=1}^N \left( 1 - SSIM \left( Net(f_i; \theta), \left( \frac{f_i}{u_i} \right) \right) \right). \quad (8)$$

In Formulas (6)~(8),  $f_i$  is the  $i$ -th image contaminated by the bias field,  $u_i$  is the corresponding real image,  $\theta$  represents the network parameter, and  $\alpha$  and  $\beta$  are the hyperparameters that control the ratio of  $Loss_{mse}$  and  $Loss_{dissim}$ . In experiment, we set  $\alpha = 1$  and  $\beta = 0.01$ .

$SSIM \left( Net(f_i; \theta), \left( \frac{f_i}{u_i} \right) \right)$  is used to measure the structural similarity between the

estimated bias field image and the desired bias field image. Its value range is [0,1], and it is a full reference image quality evaluation index [40]. Its formula is defined as follows:

$$SSIM \left( Net(f_i; \theta), \frac{f_i}{u_i} \right) = \frac{\left( 2\mu_{Net(f_i; \theta)} \mu_{\left( \frac{f_i}{u_i} \right)} + C_1 \right) \left( 2\sigma_{Net(f_i; \theta) \left( \frac{f_i}{u_i} \right)} + C_2 \right)}{\left( \mu_{Net(f_i; \theta)}^2 + \mu_{\left( \frac{f_i}{u_i} \right)}^2 + C_1 \right) \left( \sigma_{Net(f_i; \theta)}^2 + \sigma_{\left( \frac{f_i}{u_i} \right)}^2 + C_2 \right)} \quad (9)$$

where,  $C_1$  and  $C_2$  are constants. In order to avoid the denominator being 0, they are usually

set as  $C_1 = (K1 * R)^2$  and  $C_2 = (K2 * R)^2$ .  $R$  is the dynamic range of the pixel value; and generally

$K1=0.01$ ,  $K2=0.03$ , and  $R=255$  (if the image is normalized,  $R=1$ ).  $\mu_{Net(f_i;\theta)}$  and  $\mu_{(f_i/u_i)}$

respectively represent the mean value of the estimated bias field image and the desired bias field

image,  $\sigma_{Net(f_i;\theta)}$  and  $\sigma_{(f_i/u_i)}$  respectively represent the variance of the two, and

$\sigma_{Net(f_i;\theta)(f_i/u_i)}$  represents the covariance of the two.

## 4. Experimental Results and Analysis

### 4.1 Quantitative standard for bias removal

In order to evaluate the bias removal performance, in the experiments on the same dataset, our method was quantitatively evaluated and compared with the N4 and NIMS methods in terms of the structural similarity index(SSIM), coefficient of variation(CV) and joint coefficient of variation (CJV).

The SSIM is a structural similarity index that measures the similarity of two images, and its definition is shown in Formula (9). It measures the similarity between the real image and the corrected image and judges whether the bias removal is good according to the degree of similarity.

CV is the coefficient of variation of the same tissue. The smaller the CV is, the better the uniformity of an image [23]; and its calculation formula is as follows:

$$CV(T_n) = \frac{\sigma(T_n)}{\mu(T_n)} \quad (10)$$

where,  $\sigma$  and  $\mu$  respectively represent the variance and mean of the pixels in the area. In each original image and the corresponding corrected image, the CVs of the white matter and gray matter tissue regions were respectively calculated, and the quality of the bias removal in the same tissue region was determined according to the CV.

However, the coefficient of variation alone cannot provide information about the joint variation of the distribution of different tissues. When the CV of one tissue region changes and the other tissue region remains unchanged, the effect of image nonuniformity correction is still not ideal, and the joint coefficient of variation (CJV) can overcome these limitations. The calculation of the CJV, which is a direct indicator of the degree of overlap between the two tissue regions, requires two different tissue regions; and the smaller the CJV is, the better the image uniformity correction effect [38]. For two different organizational regions  $T_1$  and  $T_2$ , the calculation formula is as follows:

$$CJV(T_1, T_2) = \frac{\sigma(T_1) + \sigma(T_2)}{|\mu(T_1) - \mu(T_2)|} \quad (11)$$

BiasNet was implemented using the publicly available TensorFlow framework and Keras

artificial neural network library with Adam optimization and trained using a deep learning acceleration computing server. The server is configured with a 3.20 GHz Core i5–6500H CPU, an NVIDIA GeForce RTX 2080 (11GB) GPU and 32 GB RAM. In the training process, the learning rate was set to  $1e-3$ .

## 4.2 Results from the simulation database BrainWeb

In this paper, we first studied the performance of the proposed method on the SBD [41]. The size of each MRI brain image is  $181 \times 217 \times 181$ , and the resolution is  $1 \times 1 \times 1 \text{ mm}^3$ . Here, 2D MRI slices were extracted from the volumes with different INU levels (20%, 40%, and 60%) on the axial plane and were trained and tested respectively. We use rotation, mirroring, translation and other methods to expand the samples. Finally, for the volume of each INU level, 1359 slices were obtained for training, 151 slices were used for verification and 30 slices were used for testing. In order to further speed up the training process and obtain less redundant regions, we cropped the edge of each slice, and the slice size was  $210 \times 180$ .

In order to prove the effectiveness of the method proposed in this paper, we compared our method with the N4 and NIMS methods and performed experiments on replacing the SCR component in BiasNet with the CR component.

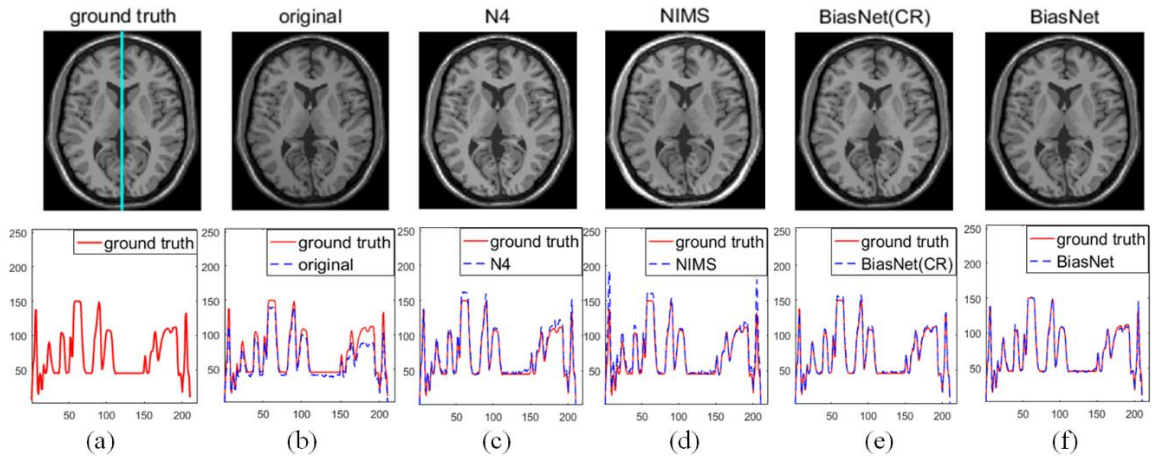


Fig. 7 The results of different methods of correction on the T1w image with 40% INU and 1% noise on the Brainweb dataset (top) and the corresponding intensity distribution comparison diagram of the 90th column (bottom). (a) Real image (b) Original image (c) Image corrected by N4 (d) Image corrected by NIMS (e) Image corrected by BiasNet (CR) (f) Image corrected by BiasNet.

In Fig. 7, we drew a comparison of the intensity distribution of the simulated T1w image with 1% noise and 40% INU before and after correction in the 90th column (along the turquoise line). Fig. 7(a) is the real image (top) and the intensity distribution diagram of the 90th column (bottom); Fig. 7(b) is the original image with 1% noise and 40% INU (top) and the intensity distribution comparison diagram of the 90th column between the original image and the real image (bottom); and Fig. 7(c)–Fig. 7(f) are the images corrected by the N4, NIMS, BiasNet (CR), and BiasNet methods (top) and the intensity distribution of the 90th column of the corrected image and the real image (bottom), respectively. The intensity distribution comparison diagram, shows that Fig. 7(f) best fits the intensity distribution of the real image, and the fitting effect of Fig. 7(e) is also better than those of Fig. 7(c) and Fig. 7(d). This shows that the proposed correction strategy is effective for intensity nonuniformity correction, while removing the multiplicative noise contained in the image and retaining the edges and

finer details in the input image.

Next, we will quantitatively evaluate the performance of BiasNet (CR), BiasNet, and the traditional state-of-the-art N4 and NIMS methods on the BrainWeb database using SSIM, CV, and CJV.

Fig. 8 shows the SSIMs with different methods on datasets with different INU and noise levels from the BrainWeb database.

In Fig. 8,  $ni - j(i = 0,1,3; j = 20,40,60)$  refers to the dataset with noise level  $i\%$  and INU  $j\%$ . Fig. 8 shows that the SSIM of the NIMS method is almost the lowest on all the tested datasets. This may be because the NIMS algorithm uses the log-Gabor filter bank to perform multiscale analysis on the input image to extract the bias field, and filtering may affect the detailed characteristics of the image; therefore the SSIM of the NIMS algorithm is low. The SSIMs of BiasNet (CR) and BiasNet are not much different, and both are better than those of N4 and NIMS. As the INU level increases, this advantage becomes more obvious.

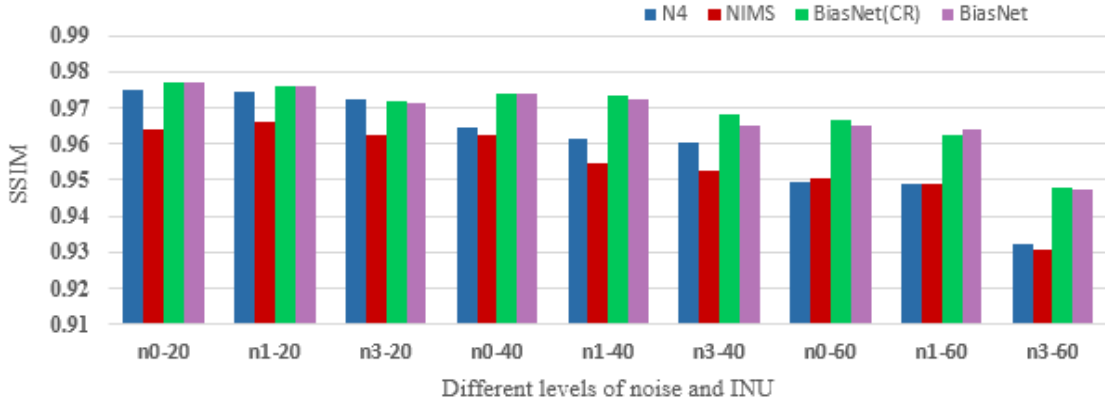


Fig. 8 De-bias measure of SSIM from different methods of with different INU and noise levels from the Brainweb database.

Table 1 CV values in gray matter (GM) on T1w axial images of SBD

Noise level(%)	INU(%)	Method				
		Original(%)	N4(%)	NIMS(%)	BiasNet(CR)(%)	BiasNet(%)
0	20	8.05±0.18	7.94±0.33	7.96±0.35	7.97±0.17	<b>7.94±0.17</b>
	40	8.46±0.22	8.09±0.35	8.09±0.37	7.99±0.25	<b>7.94±0.21</b>
	60	8.42±0.39	8.07±0.42	8.22±0.38	8.02±0.17	<b>7.80±0.26</b>
1	20	8.17±0.14	8.14±0.33	8.11±0.33	7.94±0.16	<b>7.88±0.15</b>
	40	8.59±0.20	8.16±0.43	8.11±0.40	7.99±0.15	<b>7.91±0.17</b>
	60	8.64±0.39	8.20±0.36	8.20±0.34	8.05±0.23	<b>8.03±0.24</b>
3	20	8.70±0.21	8.36±0.33	8.36±0.31	7.89±0.16	<b>7.87±0.17</b>
	40	9.00±0.29	8.51±0.31	8.49±0.32	7.98±0.21	<b>7.85±0.15</b>
	60	10.1±0.39	9.33±0.35	9.32±0.35	<b>8.02±0.33</b>	8.22±0.36

In the experiments, the performance of the proposed scheme was compared quantitatively with those of N4 and NIMS in terms of the CV and CJV. T1w images with three different noise levels (0%,

1%, and 3%) and three different INU amplitudes (20%, 40%, and 60%) from the BrainWeb database are considered for nonuniformity correction. Table 1 and Table 2 give the comparison of the CVs of the gray matter region and the white matter region before and after the T1w image correction, respectively. Table 3 provides a comparison of the CJVs of gray matter and white matter regions before and after image correction. The lower the CV is, the smaller the scattering intensity of the segmented region, which in turn indicates that the uniformity of the same tissue region is higher. Table 1 and Table 2 show that the performance of the proposed scheme is significantly better than that of the N4 and NIMS methods. Especially in the case of a high noise level and high INU amplitude, the performance advantage of our method is more obvious. Of course, effective bias field correction should increase the contrast of the image, which can be reflected by the appropriate separation of the peaks of the white matter and gray matter distribution or characterized by a sharp drop in the CJV. Table 3 shows that under high noise levels, the CJVs of the BiasNet (CR) and BiasNet are significantly reduced, indicating that the separation of the intensity level of the white matter and gray matter tissue regions is improved. The quantitative analysis of the SSIM, CV, and CJV shows that the scheme proposed in this paper is effective at correcting the bias field under the condition of a higher noise level and INU amplitude.

Table 2 CVs in white matter (WM) on T1w axial images of SBD

Noise level(%)	INU(%)	Method				
		Original(%)	N4(%)	NIMS(%)	BiasNet(CR)(%)	BiasNet(%)
0	20	4.54±0.40	4.32±0.32	4.37±0.34	4.14±0.62	<b>4.12±0.52</b>
	40	5.37±0.32	4.29±0.38	4.31±0.39	4.26±0.40	<b>4.15±0.56</b>
	60	5.71±0.31	4.51±0.30	4.83±0.36	4.60±0.32	<b>4.43±0.50</b>
1	20	4.60±0.39	4.29±0.27	4.26±0.32	4.13±0.47	<b>4.11±0.54</b>
	40	5.45±0.27	4.50±0.63	4.43±0.56	4.30±0.46	<b>4.25±0.65</b>
	60	5.96±0.38	4.68±0.24	4.69±0.25	4.73±0.37	<b>4.65±0.39</b>
3	20	5.44±0.36	4.69±0.31	4.66±0.30	4.37±0.42	<b>4.48±0.46</b>
	40	6.03±0.36	4.82±0.24	4.80±0.21	4.64±0.51	<b>4.61±0.41</b>
	60	7.27±0.54	6.04±0.41	6.01±0.43	5.07±0.46	<b>4.99±0.56</b>

Table 3 Coefficients of joint variation (CJVs) on T1w axial images of SBD.

Noise level(%)	INU(%)	Method				
		Original(%)	N4(%)	NIMS(%)	BiasNet(CR)(%)	BiasNet(%)
0	20	44.4±3.36	43.5±2.16	44.1±2.15	42.9±3.67	<b>42.9±3.36</b>
	40	48.7±2.97	44.8±2.26	45.1±2.31	43.4±3.23	<b>43.3±3.17</b>
	60	51.7±2.92	45.9±1.89	47.4±2.03	46.1±3.45	<b>45.2±2.65</b>
1	20	45.1±3.19	44.5±2.38	44.5±2.28	43.4±3.31	<b>43.4±3.23</b>
	40	49.3±3.00	45.9±2.88	45.6±2.52	44.0±3.33	<b>43.9±3.56</b>
	60	53.3±3.21	48.0±2.60	47.8±2.62	46.3±2.90	<b>46.3±2.67</b>
3	20	50.3±3.45	47.5±2.41	47.5±2.37	<b>44.6±3.20</b>	45.8±3.07
	40	53.6±3.54	49.0±2.05	49.0±2.00	<b>46.1±3.49</b>	47.1±3.16
	60	64.8±4.18	57.9±5.62	57.9±5.58	51.7±2.88	<b>49.9±3.30</b>

Fig. 9 shows the correction results obtained after applying the BiasNet method to BrainWeb simulation data with different noise levels and INU amplitudes. Fig. 9(a) shows the T1w axial image

degraded by 20% INU (1% noise), Fig. 9(d) shows the T1w axial image degraded by 40% INU (no noise), and Fig. 9(b) ~ Fig. 9 (c) and Fig. 9 (e) ~ Fig. 9 (f) correspond to the predicted bias fields and corrected images, respectively. Through visual inspection, it can be clearly seen that the BiasNet method can effectively remove the bias field, and the intensity change of white matter tissue area is significantly reduced in the corrected image.

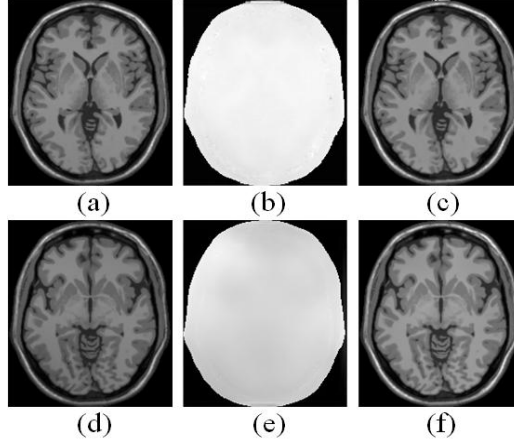


Fig. 9 The correction result of the BiasNet method on the BrainWeb dataset. (a)~(c) Original image (20% INU, 1% noise), predicted bias field, corrected image (d)~(f) Original image (40% INU, no noise), predicted bias field, corrected image.

### 4.3 Results from the real database HCP

The model proposed in this paper is verified on real human brain MR images of the HCP (Human Connectome Project) [42] dataset. The dataset contains T1w and T2w structure MR images of healthy adults from a Siemens Skyra 3T scanner and contains the bias fields of the corresponding images. For specific details, please refer to the literature [43]. In the experiment, we randomly selected the T1w structure images of 10 patients in the dataset. The size of each MRI brain image was  $260 \times 311 \times 260$  voxels and the resolution was  $0.7 \times 0.7 \times 0.7$  mm<sup>3</sup>. We randomly selected 1000 slices from these 10 brain image volumes. In order to train the model better, we expanded the data using rotation and mirroring methods, and finally obtained 2880 training samples, 320 verification samples, and 200 test samples. Similarly, in order to speed up the training process and obtain fewer redundant regions, we cropped the edges of the images, and the size of each sample was  $300 \times 240$ .

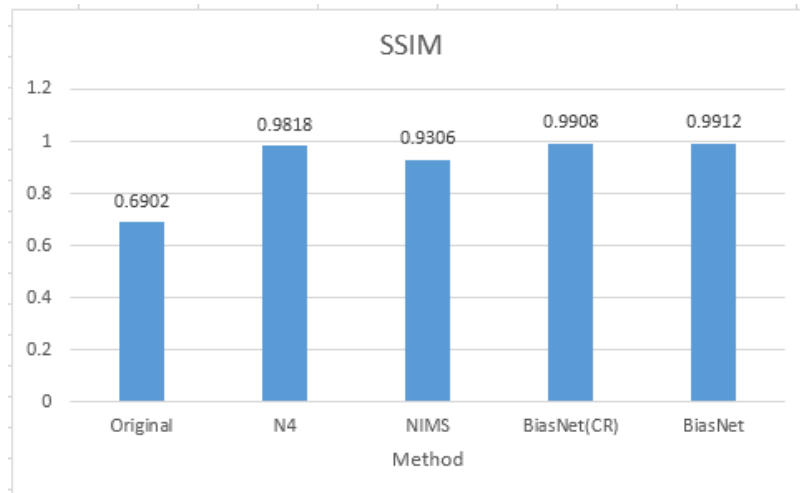


Fig. 10 The de-bias measures of SSIM of different methods from the HCP dataset

Fig. 10 shows the SSIMs obtained after correction with different methods. It can be seen from Fig. 10 that the proposed scheme in this paper also shows good performance on the real human brain dataset. Fig.11 clearly shows that in the original image, the intensity of the white matter region along the selected line highlighted in turquoise has changed very obviously due to the bias field. After correction using the BiasNet method, the white matter intensity variation of approximately 0.25 in the normalized original image is reduced to less than 0.15.

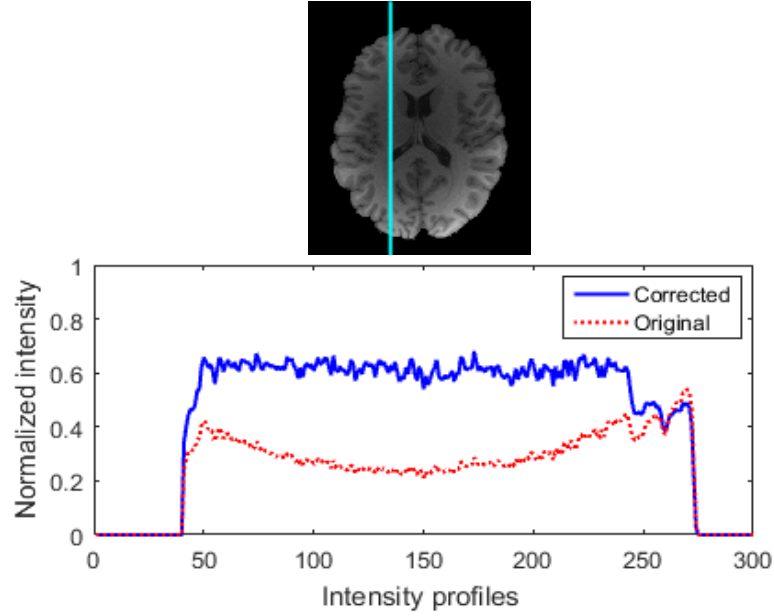


Fig. 11 Comparison of intensity distribution along the selected line displayed in the T1w axial image before and after correction

In the test samples, the CVs before and after correction were calculated with the proposed model to evaluate the intraclass changes in white matter and gray matter tissue regions. Table 4 shows the average CV of 200 test samples. Although both the N4 and NIMS algorithms reduce the CVs of gray and white matter in the images, the model proposed in this paper is more effective than these two algorithms. The average CJVs between white matter and gray matter are also listed in Table 5. Table 5 shows that after correction with the BiasNet model, the CJV between white matter and gray matter in the image drops to 64% of the initial value. In the same situation, the N4 and NIMS methods can only be reduced to approximately 77% of the initial value. Obviously, on the real human brain image dataset, the performance of the scheme proposed in this paper is also better than the N4 and NIMS methods in the three aspects of the SSIM, CV and CJV.

Table 4 Coefficient of variation on the HCP real dataset

	Original(%)	Corrected			BiasNet(%)
		N4(%)	NIMS(%)	BiasNet(CR)(%)	
GM	18.8±0.69	18.6±1.77	17.8±1.86	16.9±0.46	<b>16.5±0.76</b>
WM	15.0±0.83	10.6±0.66	10.4±0.86	6.58±0.74	<b>6.41±0.54</b>

Table 5 Coefficient of joint variation on the HCP real dataset

Original(%)	Corrected			
	N4(%)	NIMS(%)	BiasNet(CR)(%)	BiasNet(%)
83.4±3.82	63.9±2.50	65.2±1.60	55.2±6.88	<b>53.4±2.77</b>

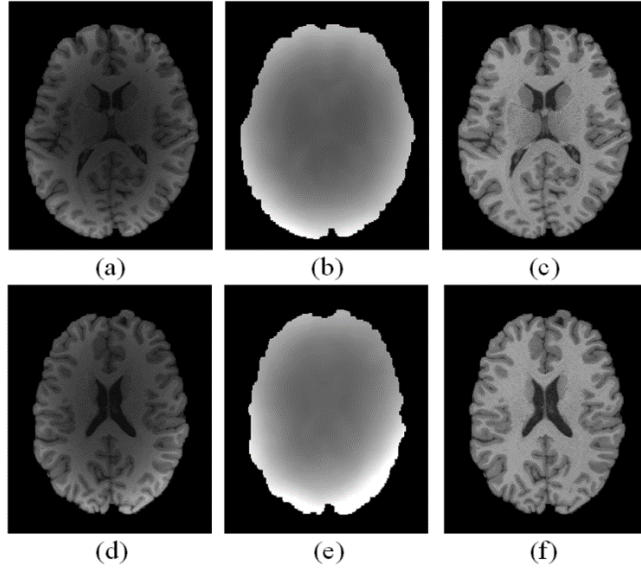


Fig. 12 The correction results of BiasNet on the slices of two different patients. (a), (d) original image (b), (e) predicted bias field (c), (f) corrected image.

Fig. 12 shows the corrected results of the BiasNet method on two randomly selected slices of different patients. It can be observed from Fig. 12 that the predicted bias field is smooth, and the intensity of each tissue region of the corrected image looks more consistent, which is obvious in the white matter regions in Fig. 12(c) and Fig. 12(f). Therefore, the effectiveness of the proposed scheme for the correction of intensity inhomogeneity in clinical data is visually verified.

#### 4.4 Experiment results on 3D images

On the HCP [42] dataset, we further verified the model proposed in this paper on 3D data. From the dataset, we randomly selected T1w structure images of 179 patients, of which 139 samples were used for training, 20 samples were used for verification, and 20 samples were used for testing. In order to speed up the training process and obtain fewer redundant regions, we cropped each MRI brain image volume to  $256 \times 304 \times 256$ , and divided the image into patches. In order to better reduce the memory burden, we used  $64 \times 64 \times 64$  voxel patches. By using a sliding window strategy with a stride of  $48 \times 48 \times 48$ , a total of 20850 patches were obtained for training, and 3000 patches were used for verification. In the test stage, in order to eliminate the patch boundary artifacts, we changed the stride of the sliding window to  $24 \times 24 \times 24$ , so that 17820 patches could be obtained, and the trained network was applied to the patches of the test set. We performed an averaging operation on the predicted values of the overlapping regions of the patches. We trained our two different models for 10 epochs, with a learning rate of  $1e-3$  and optimized the models with Adam.

Table 6 Comparison of BiasNet (2D) and BiasNet (3D) on the HCP database

Method	CV(%)		CJV(%)	SSIM
	GM	WM		
Original	18.8±0.69	15.0±0.83	83.4±3.82	0.6902
BiasNet(2D)	<b>16.5±0.76</b>	6.41±0.54	53.4±2.77	<b>0.9912</b>
BiasNet(3D)	16.9±0.98	<b>6.36±0.46</b>	<b>51.1±2.64</b>	0.9728

Table 6 shows the experimental results of the quantitative evaluation of BiasNet based on two-dimensional slices and three-dimensional patches. The corresponding boxplots of the CV and CJV are

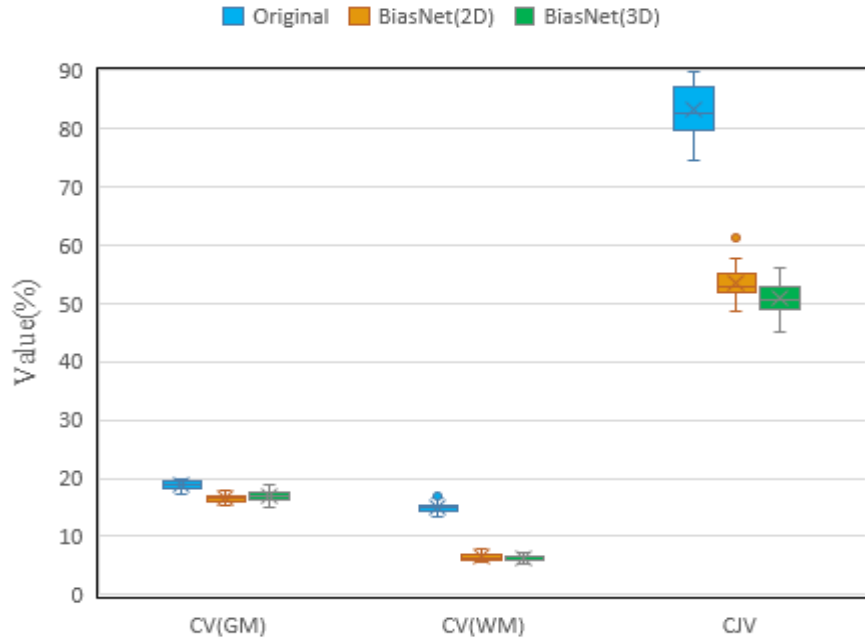


Fig. 13 The boxplot of the CV for gray matter and white matter, and the boxplot of the CJV between gray matter and white matter.

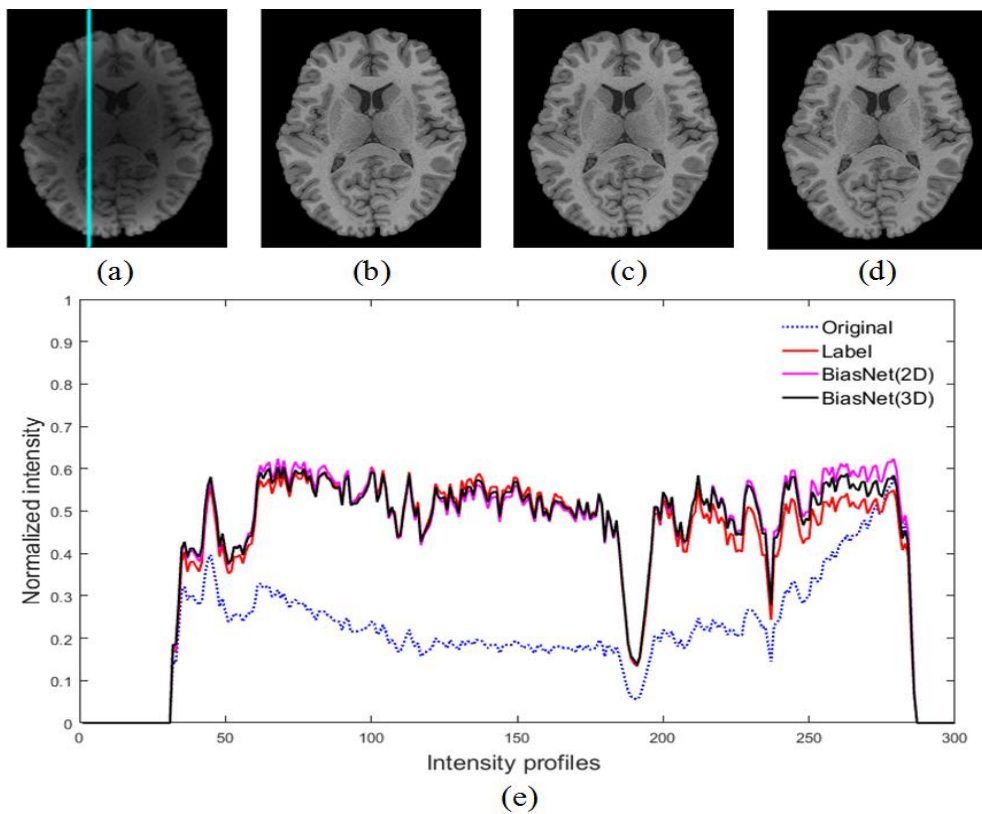


Fig. 14 Comparison of the correction results of BiasNet (2D) and BiasNet (3D) on the HCP database. (a) Original image (b) Real image (c) BiasNet(2D) (d) BiasNet(3D) (e) Comparison of intensity distribution in column 90.

shown in Fig. 13. It can be seen from Table 6 that in terms of CVs, BiasNet (2D) and BiasNet (3D) both show superior correction performance, especially for the visible high-intensity changes in the

white matter tissue regions in the image that were effectively quantitatively corrected by reducing the CVs in the white matter. The CJVs between white matter and gray matter are also listed in Table 6. The CJV can better reflect the gray uniformity of an entire image. BiasNet (3D) considers more spatial information and shows better performance in the quantitative evaluation of the CJV. The boxplot in Fig. 13 depicts the same situation. Since BiasNet (3D) is trained based on patches, there may be boundary effects after the patches are stitched, resulting in the SSIM of BiasNet (3D) being lower than that of BiasNet (2D).

Fig. 14 shows a comparison of the results of a patient after correction using BiasNet (2D) and BiasNet (3D). From a visual point of view, there is little difference between Fig. 14(c) and Fig. 14(d), but from the intensity distribution of the 90th column, the intensity distribution of BiasNet (3D) fits better with that of the real image.

#### 4.5 The influence of Log-Gabor features on bias removal

On the  $n1-20$ ,  $n1-40$ , and  $n1-60$  datasets of the BrainWeb database, we removed the log-Gabor features of three scales and used the BiasNet model for training. The experimental results on the test set are shown in Table 7.

Table 7 Comparison of BiasNet (no log-Gabor) and BiasNet on SBD

	BiasNet(no Log-Gabor)			SSIM	BiasNet			
	CV(%)		CJV(%)		CV(%)		CJV(%)	SSIM
	GM	WM			GM	WM		
$n1-20$	$7.96\pm 0.19$	$4.30\pm 0.43$	$43.6\pm 3.10$	0.9753	<b><math>7.88\pm 0.15</math></b>	<b><math>4.11\pm 0.54</math></b>	<b><math>43.4\pm 3.23</math></b>	<b>0.9758</b>
$n1-40$	$8.01\pm 0.22$	$4.50\pm 0.31$	$45.1\pm 3.05$	0.9695	<b><math>7.91\pm 0.17</math></b>	<b><math>4.25\pm 0.65</math></b>	<b><math>43.9\pm 3.56</math></b>	<b>0.9723</b>
$n1-60$	$8.18\pm 0.22$	$5.69\pm 0.43$	$51.6\pm 1.45$	0.9564	<b><math>8.03\pm 0.24</math></b>	<b><math>4.65\pm 0.39</math></b>	<b><math>46.3\pm 2.67</math></b>	<b>0.9643</b>

Table 7 shows that after adding log-Gabor features of different scales in training, the CVs, CJVs, and SSIMs have been improved to varying degrees. The greater the INU amplitude is, the more obvious this advantage. When the INU amplitude is 20%, after the introduction of the log-Gabor feature, the CJV decreases by 0.2; and when the INU amplitude is 60%, after the introduction of log-Gabor feature, the value of CJV decreases from  $51.6\pm 1.45$  to  $46.3\pm 2.67$ . Therefore, in the process of extracting the bias field, log-Gabor features of different scales can provide additional local information of the bias field.

### 5. Discussion and Conclusion

In this paper, we propose a new method for the bias removal of MR brain images based on deep convolutional neural networks. This bias field correction method based on deep learning does not require segmentation of the scanner or the subject or any prior knowledge, and it is a multi-input network combined with residual learning. The log-Gabor filter bank is used for multiscale analysis of an input image to extract the local feature maps of the bias field in multiple frequency bands. The local feature maps and the original image are simultaneously sent to BiasNet, so that BiasNet can automatically learn in depth to obtain the bias field. In addition, we designed the SCR component to extract more local features. Compared with the CR component, the SCR component can obtain a more accurate bias field.

The performance of BiasNet was tested on the BrainWeb database and HCP dataset, and the results showed that the performance of BiasNet was better than the performances of the traditional

state-of-the-art N4 and NIMS methods.

In the white matter and gray matter regions, the performance of the method proposed in this paper was quantitatively evaluated on the simulated BrainWeb database using the CV. The intraclass variation of the decrease in intensity level observed in the qualitative analysis was verified by experiments. Regardless of the noise level and INU amplitude, the experimental results show that the CJV is also significantly reduced. The quantitative evaluations of the SSIM, CV, and CJV given in Fig.8, Table 1, Table 2 and Table 3 reveal that the performance of BiasNet is better than those of the N4 and NIMS methods, especially in the case of higher levels of noise and INU in the simulated data. On the HCP real dataset, after image correction, the significant decrease in the ratio of the CV and CJV indicates that the interclass separation of white matter and gray matter tissue regions has been improved and the intraclass intensity changes have been reduced. The small improvement of the SSIM shows that the images corrected by our method are more structurally similar to the real images. Compared with N4 and NIMS, BiasNet produces higher SSIMs and lower CVs and CJVs. In addition, we also performed 3D experiments on the HCP dataset. Table 6 shows that compared with the slice-based 2D experimental results, the CJV of BiasNet (3D) decreases significantly, which indicates that the gray matter and white matter separation is better on the 3D level. However, the SSIM has decreased due to the boundary effect that occurs when the patches are stitched.

In our work, the SSIM is low due to the boundary effect in the experiment on 3D data. Next, we will study setting different weights for each patch to reduce the boundary effect that occurs during image stitching. In addition, another key limitation of our method is the need for high-quality unbiased ground-truth images from real datasets, which are difficult to obtain in practical applications. How to improve the image analysis performance by combining prior knowledge of organ shapes and locations is not obvious in recent deep learning techniques [44]. Oktay et al. used a new regularization model to integrate anatomical prior knowledge into a CNN for end-to-end learning in 2018. They showed that the method can not only be easily adapted to different analysis tasks (such as image segmentation and enhancement) but can also improve the accuracy of the prediction model [44]. Therefore, in future work, we will combine prior knowledge such as anatomy and residuals and use special learning techniques, such as transfer learning, to reduce future unsupervised bias removal tasks.

In conclusion, the multi-input bias removal convolutional neural network method based on deep learning proposed in this paper can not only accurately estimate the bias fields in MR images, but also effectively retain the detailed MR brain image structure, which can provide high-quality MR images with uniform intensity distribution for subsequent image analysis tasks (such as segmentation, registration, etc.).

## Acknowledgments

This work was supported in part by the National Natural Science Foundation of China under Grant 61771230, Grant 61903229 and Grant 61973180, and in part by the Natural Science Foundation of Shandong Province of China under Grant ZR2019BF004, Grant ZR2019PF005, and Grant ZR2020QF011.

## Declarations

**Conflict of interest** The authors declare that they have no conflict of interest.

**Ethical approval** All procedures performed in studies involving human participants were in accordance with the ethical standards of the institutional and/or national research committee and with the 1975 Declaration of Helsinki and its later amendments or comparable ethical standards.

**Human and animal rights** This article does not contain any studies with human participants or animals performed by any of the authors.

### **Informed consent**

Informed consent was obtained from all individual participants included in the study.

## References

- [1] Z. Hou, "A Review on MR Image Intensity Inhomogeneity Correction.," *International journal of biomedical imaging*, 2006(1), 49515, (2006).
- [2] D. A. G. Wicks, G. J. Barker and P. S. Tofts, "Correction of intensity nonuniformity in MR images of any orientation," *Magnetic Resonance Imaging*, 11(2), 183–196, (1993).
- [3] B. R. Condon, J. Patterson and D. J. Wyper, "Image non-uniformity in magnetic resonance imaging: its magnitude and methods for its correction," *The British journal of Radiology*, 60(709), 83–87, (1987).
- [4] X. Li, L. Li, H. Lu, and Z. Liang, "Partial volume segmentation of brain magnetic resonance images based on maximum a posteriori probability," *Medical Physics*, 32(7), 2337–2345, (2005).
- [5] V. A. F. P. Uroš, "MRI intensity inhomogeneity correction by combining intensity and spatial information," *Physics in Medicine and Biology*, 49(17), 4119–4133, (2004).
- [6] Collewet, G., Davenel, A., Toussaint, C., & Akoka, S. Correction of intensity nonuniformity in spin-echo t 1-weighted images. *Magnetic resonance imaging*, 20(4), 365–373, (2002).
- [7] Brey, W. W., & Narayana, P. A. Correction for intensity falloff in surface coil magnetic resonance imaging. *Medical Physics*, 15(2), 241–245, (1988).
- [8] Narayana, P., Brey, W., Kulkarni, M., & Sievenpiper, C. Compensation for surface coil sensitivity variation in magnetic resonance imaging. *Magnetic resonance imaging*, 6(3), 271–274, (1988).
- [9] SONG, Shuang; ZHENG, Yuanjie; HE, Yunlong. A review of Methods for Bias Correction in Medical Images. *Biomedical Engineering Review*, 1(1), 1–10, (2017).
- [10] Lewis, E. B., & Fox, N. C. Correction of differential intensity inhomogeneity in longitudinal mr images. *Neuroimage*, 23(1), 75–83, (2004)..
- [11] Cohen, M. S., DuBois, R. M., & Zeineh, M. M. (2000). Rapid and effective correction of rf inhomogeneity for high field magnetic resonance imaging. *Human brain mapping*, 10(4), 204–211
- [12] Dawant, B. M., Zijdenbos, A. P., & Margolin, R. A. Correction of intensity variations in mr images for computer-aided tissue classification. *IEEE transactions on medical imaging*, 12(4), 770–781, (1993).
- [13] Brechbühler, C., Gerig, G., & Székely, G. Compensation of Spatial Inhomogeneity in MRI

Based on a Parametric Bias Estimate. *Visualization in Biomedical Computing, 4th International Conference, VBC '96, Hamburg, Germany, September 22-25, 1996, Proceedings*, (1996).

[14] Styner, M., Brechbuhler, C., Szckely, G., & Gerig, G. Parametric estimate of intensity inhomogeneities applied to mri. *IEEE transactions on medical imaging*, 19(3), 153–165, (2000).

[15] Milles, J., Zhu, Y. M., Gimenez, G., Guttman, C. R., & Magnin, I. E.. Mri intensity nonuniformity correction using simultaneously spatial and gray-level histogram information. *Computerized Medical Imaging and Graphics*, 31(2), 81–90, (2007).

[16] Li, C., Huang, R., Ding, Z., Gatenby, J. C., Metaxas, D. N., & Gore, J. C. A level set method for image segmentation in the presence of intensity inhomogeneities with application to mri. *IEEE Transactions on Image Processing*, 20(7), 2007–2016, (2011).

[17] Li, C., Gore, J. C., & Davatzikos, C. Multiplicative intrinsic component optimization (mico) for mri bias field estimation and tissue segmentation. *Magnetic resonance imaging*, 32(7), 913–923, (2014).

[18] Xie, M., Gao, J., Zhu, C., & Zhou, Y.. A modified method for mrf segmentation and bias correction of mr image with intensity inhomogeneity. *Medical & biological engineering & computing*, 53(1), 23–35, (2015).

[19] Banerjee, A., & Maji, P. Rough sets and stomp normal distribution for simultaneous segmentation and bias field correction in brain mr images. *IEEE Transactions on Image Processing*, 24(12), 5764–5776, (2015).

[20] Sled, J. G., Zijdenbos, A. P., & Evans, A. C. A nonparametric method for automatic correction of intensity non-uniformity in mri data. *IEEE transactions on medical imaging*, 17(1), 87–97, (1998).

[21] Mangin, J.-F. Entropy Minimization for Automatic Correction of Intensity Nonuniformity. *Mathematical Methods in Biomedical Image Analysis*, 2000. Proceedings. IEEE Workshop on IEEE, 162–169, (2000).

[22] Milles, J., Zhu, Y. M., Gimenez, G., Guttman, C. R., & Magnin, I. E. Mri intensity nonuniformity correction using simultaneously spatial and gray-level histogram information. *Computerized Medical Imaging and Graphics*, 31(2), 81–90, (2007).

[23] Vovk U, Pernus F, Likar B. A Review of Methods for Correction of Intensity Inhomogeneity in MRI[J]. *IEEE Transactions on Medical Imaging*, 26(3), 405-421, (2007).

[24] Tustison NJ, Avants BB, Cook PA, Zheng Y, Egan A, Yushkevich PA, et al. N4ITK: improved N3 bias correction. *IEEE Trans Med Imaging*, 6(29), 1310–1320, (2010).

[25] Hui Liu, Shanshan Liu Dongmei Guo, et al. Original intensity preserved inhomogeneity correction and segmentation for liver magnetic resonance imaging[J]. *Biomedical Signal Processing and Control*, (47), 231-239, (2019).

[26] George M M, Kalaivani S, Sudhakar M S. A non-iterative multi-scale approach for intensity inhomogeneity correction in MRI [J]. *Magnetic Resonance Imaging*, (42), 43-59, (2017).

[27] Lucas, A., Iliadis, M., Molina, R., Katsaggelos, A. K. Using deep neural networks for inverse problems in imaging: beyond analytical methods. *IEEE Signal Processing Magazine* 35(1), 20–36, (2018).

[28] Xiao Zhitao, Guo Chengming, Yu Ming, et al. Application of log Gabor function in the research of human visual system characteristics[J]. *Signal Processing*, 18(005), 399-402, (2002).

[29] Field DJ. Relations between the statistics of natural images and the response properties of cortical cells. *J Opt Soc Am A*, 4( 12) , 2379–2394, (1987).

[30] KOVESI D P . What are Log-Gabor filters and why are they good ? [ EB

/OL ]. <http://www.csse.uwa.edu.au/~pk/research/matlabfns/PhaseCongruency/Docs/convexpl.html>, (2006).

[31] Chen Xiao. Research on visual feature extraction based on Gabor transform [D]. Jilin: School of Software, Jilin University, (2010).

[32] Chao H, Hatsukami T S , Yuan C . A multi - scale method for automatic correction of intensity non - uniformity in MR images[J]. Journal of Magnetic Resonance Imaging Jmri, 2001, 13(3), 428-436, (2001)

[33] LeCun, Y., Bengio, Y., Hinton, G.: Deep learning. Nature 521(7553), 436–444, (2015).

[34] K. Zhang, W. Zuo, Y. Chen, D. Meng, and L. Zhang, “Beyond a Gaussian denoiser: residual learning of deep CNN for image denoising,” IEEE Transactions on Image Processing, 26(7), 3142–3155, (2017).

[35] Dong C., Loy C.C., He K., Tang X. Learning a deep convolutional network for image super-resolution: European Conference on Computer Vision, Springer, (8692), 184-199, (2014).

[36] Pham DL, Prince JL. Adaptive fuzzy segmentation of magnetic resonance images. IEEE Trans Med Imaging, 18(9), 737–752, (1999).

[37] [1] Shattuck D W , Sandor-Leahy S R , Schaper K A , et al. Magnetic resonance image tissue classification using a partial volume model.[J]. Neuroimage, 13(5), 856-876, (2001).

[38] Gholizadeh-Ansari M , Alirezaie J , Babyn P . Low-dose CT Denoising with Dilated Residual Network[C], in Proceedings of the 2018 40<sup>th</sup> Annual International Conference of the IEEE Engineering in Medicine and Biology Society (EMBC), 5117–5120, (2018).

[39] K. He, X. Zhang, S. Ren and J. Sun, "Deep Residual Learning for Image Recognition," 2016 IEEE Conference on Computer Vision and Pattern Recognition (CVPR), 770-778, (2016).

[40] Xu Y, Hu S , Du Y . Bias Correction of Multiple MRI Images Based on an Improved Nonparametric Maximum Likelihood Method[J]. IEEE Access, 7(1):166762-166775, (2019).

[41] Cocosco C A , Kollokian V , Kwan K S , et al. BrainWeb: Online Interface to a 3D MRI Simulated Brain Database[J]. NeuroImage, 5(4), (1997).

[42] Van Essen DC, Smith SM, Barch DM, Behrens TEJ, Yacoub E, Ugurbil K. The WUMinn human connectome project: an overview. Neuroimage, 80(80), 62–79, (2013).

[43] WU-Minn HCP. 900 Subjects data release: reference manual, (2015).

[44] O. Oktay, E. Ferrante, K. Kamnitsas et al., Anatomically Constrained Neural Networks (ACNN): Application to Cardiac Image Enhancement and Segmentation[J]. IEEE Transactions on Medical Imaging, 37(2), 384–395, (2018).